Available online at www.sciencedirect.com

ScienceDirect

Journal of the European Ceramic Society 35 (2015) 4039–4049

www.elsevier.com/locate/jeurceramsoc

Zirconia-based composites for biomedical applications: Role of second phases on composition, microstructure and zirconia transformability

Marta Fornabaio [a,*], Paola Palmero [a], Rebecca Traverso [a], Claude Esnouf [b], Helen Reveron [b], Jérôme Chevalier [b,c], Laura Montanaro [a]

[a] Department of Applied Science and Technology, INSTM R.U. PoliTO, LINCE Lab., Politecnico di Torino, Corso Duca degli Abruzzi, 24, 10129, Torino, Italy
[b] Université de Lyon, INSA de Lyon, MATEIS UMR CNRS 5510, Bât. Blaise Pascal 7, Av. Jean Capelle, 69621 Villeurbanne, France
[c] Institut Universitaire de France, 103 bd Saint-Michel, Paris 75005, France

Available online 27 May 2015

Abstract

In order to develop ceria-stabilized zirconia (Ce-TZP) ceramics suitable for biomedical applications, composite materials should be developed. In this work, three different Ce-TZP-based composites were prepared by adding rounded α-Al_2O_3 grains and two kinds of elongated particles, $SrAl_{12}O_{19}$ and $CeMgAl_{11}O_{19}$. Composite powders were prepared through a surface coating route, which allowed a precise tailoring of chemical and phase composition as revealed by HRTEM. A limited cerium diffusion inside zirconia grains was revealed when $CeMgAl_{11}O_{19}$ was added to zirconia matrix. The role of second phases on the sintering behaviour, microstructural development and zirconia transformability was investigated. Second phases, particularly Al_2O_3, induce a delay in the zirconia densification. However, all composites presented a highly homogeneous and very fine microstructure. Strong differences in the morphologic features of the elongated grains between $CeMgAl_{11}O_{19}$ and $SrAl_{12}O_{19}$ were evidenced by FESEM. Vickers indentations hinted a strong difference in the efficiency of *t–m* transformation among the composites.

Keywords: Zirconia-based composites; Alumina; Hexaluminate; Microstructure; Sintering behaviour; Phase transformation

1. Introduction

The application of zirconia-based materials in the biomedical field, especially in dentistry, is currently increasing. The stress-induced phase transformation from the tetragonal phase to the monoclinic one implies an important volume expansion (∼4%) which hinders cracks propagation, thus contributing to the strength and toughness of tetragonal zirconia polycrystals (TZP) [1]. Among the several TZP systems, the mostly used materials are yttria-stabilized zirconia (Y-TZP) and ceria-stabilized zirconia (Ce-TZP). Y-TZP shows very high strength and moderate toughness; however, some compositions (such as 3Y-TZP) are sensitive to low temperature degradation (LTD) [2]. This phenomenon causes loss of strength and generation of micro-cracking in presence of water. On the contrary, Ce-TZP shows extremely high toughness but limited strength due to the difficulty of producing dense Ce-TZP materials with small grain size (<0.5 μm) [3]. The presence of ceria, in fact, induces a significant grain growth of zirconia during natural sintering. On the other side, innovative sintering techniques, such as spark plasma sintering or hot isostatic pressing, can be hardly applied since Ce^{4+} ions easily reduce to Ce^{3+} with a negative effect on the zirconia stability [4,5]. Thus, in order to refine the microstructure, Ce-TZP-based composites are needed. Nawa et al. showed that the addition of 30 vol% α-Al_2O_3 into a TZP matrix stabilized by 10 mol% of ceria (referred to as 10Ce-TZP) gives rise to an interpenetrated, intra-granular nanostructure with excellent results in terms of mechanical response [6]. This system is currently available on the dental market with the trade name of NANOZR [7]. By replacing alumina with 16 vol% of $MgAl_2O_4$, Apel et al. recently obtained a microstructure in which zirconia and spinel grains were about 0.5 and 0.2 μm in size, respectively, characterized by impressive mechanical properties (fracture toughness of 15 MPa and bending strength of 900 MPa) [8]. Both these systems are characterized by an equiaxial morphology of the second-phases. A further approach was proposed by Cutler and co-workers [9] concerning the addition of elongated second-phase grains able to further increase the fracture toughness

* Corresponding author. Tel.: +39 0110904678.
E-mail address: marta.fornabaio@polito.it (M. Fornabaio).

http://dx.doi.org/10.1016/j.jeurceramsoc.2015.04.027
0955-2219/

by additional bridging/crack deflection mechanisms. Strontium hexaluminate ($SrAl_{12}O_{19}$) platelets and α-alumina were developed in situ in a Ce-TZP matrix, by a solid state reaction during sintering between strontium oxide and alumina, leading to the formation of plate-like aluminates. As a consequence, a fracture toughness increase was observed. Later, several elongated aluminate phases were added to Ce-TZP systems such as barium hexaluminate ($BaAl_{12}O_{19}$), lanthanum hexaluminate ($LaAl_{11}O_{18}$), cerium hexaluminate ($CeAl_{11}O_{18}$) and also more complex, quasi-ternary aluminates, such as $BaMnAl_{11}O_{18}$ or $CeMnAl_{11}O_{19}$ [10–14]. Fracture mechanisms of three different bi-phasic Ce-TZP composites, containing respectively α-Al_2O_3, $LaAl_{11}O_{18}$ and $SrAl_{12}O_{19}$, were recently compared by Kern [15], pointing out that the toughening characteristics depend on the type of the hexaluminate phase and on the sintering conditions. The three composites presented similar zirconia grain size but different features regarding the hexaluminate phases. In fact, $LaAl_{11}O_{18}$ showed slightly higher aspect ratio and broader size distribution as compared to $SrAl_{12}O_{19}$ grains. In addition, $LaAl_{11}O_{18}$ gave rise to stronger interfaces between rods and matrix as compared to $SrAl_{12}O_{19}$, thus leading to different kinds of interaction of the crack with the reinforcements.

What is here described highlights that the achievement of excellent mechanical and physical properties required for biomedical applications can be only reached by carefully tailoring the microstructure/architecture and composition of the final composite. This requires a rigorous control of any step of manufacturing, from the synthesis of composite powders to sintering. For fulfilling such requirements, in this work we have developed three 10Ce-TZP-based composites (differing in the nature of second-phases) through a surface coating route. The effectiveness of this method in the precise and simultaneous tuning of many compositional (i.e. the ceria amount inside the zirconia phase, the stoichiometry and purity of the second phases) and microstructural (i.e. the grain size, and distribution of the phases) features in the final composite structures has been recently demonstrated by the Authors [16]. Both equiaxial α-Al_2O_3 and two kinds of aluminate phases, namely $SrAl_{12}O_{19}$ and $CeMgAl_{11}O_{19}$, were selected as second-phases, leading to bi-phasic (ZrO_2–Al_2O_3) and tri-phasic (ZrO_2–Al_2O_3–$SrAl_{12}O_{19}$ and ZrO_2–Al_2O_3–$CeMgAl_{11}O_{19}$) composites. To the best of our knowledge, few data have been so far reported about the role of the second-phases on the composite architecture and sintering behaviour of Ce-TZP materials. For this reason, we have here investigated densification behaviour, phase and microstructural development as well as stress-induced transformability of three zirconia-based systems, with the aim of developing new composites having tailored microstructural and compositional features suitable for biomedical applications.

2. Materials and methods

2.1. Materials

A commercial 10 mol% ceria-stabilized zirconia powder (supplied by Daiichi Kigenso Kagaku Kogio Co. Ltd, Japan) was employed as raw material to develop bi- and tri-phasic composite powders. 10Ce-TZP powder has a specific surface area of 14.3 m^2/g and a particle size, estimated by laser diffraction method, in the range 0.5–1 μm, as declared by the supplier [17].

For the second phases, $Al(NO_3)_3{\cdot}9H_2O$ (>98% purity), $Sr(NO_3)_2$ (>99.0% purity), $(NH_4)_2[Ce(NO_3)_6]$, (≥98.5% purity) and $Mg(NO_3)_26H_2O$ (99% purity), all supplied by Sigma–Aldrich, were used as aluminium, strontium, cerium and magnesium precursors, respectively. Precisely, the composite containing α-Al_2O_3 and $SrAl_{12}O_{19}$ phases was prepared by adding aluminium and strontium nitrate (in 1:0.022 weight ratio) to 10Ce-TZP. The composite containing α-Al_2O_3 and $CeMgAl_{11}O_{19}$ phases was obtained by adding aluminium, cerium and magnesium nitrates (in 1:0.0576:0.027 weight ratio) to 10Ce-TZP powder.

2.2. Elaboration of the composite powders

For the bi-phasic composite, 16 vol% of α-Al_2O_3 was added to the 10Ce-TZP matrix. It is referred to as ZA_{16}.

For the tri-phasic composites, two systems, differing in the composition of the elongated phase, were investigated. In the former composite (referred to as ZA_8Sr_8), 8 vol% of α-Al_2O_3 and 8 vol% of $SrAl_{12}O_{19}$ were added to 10Ce-TZP; in the latter (referred to as ZA_8Mg_8), 8 vol% of α-Al_2O_3 and 8 vol% of $CeMgAl_{11}O_{19}$ were added to the zirconia matrix.

The composite powders have been prepared by a *surface coating route*, being this process already used by the Authors for the elaboration of alumina- and zirconia-based composites [16,18]. The whole process is schematized in Fig. 1. The bold character is used to evidence the main critical steps of the process, namely the dispersion of zirconia powder, the pH of the suspension and the drying step. A zirconia aqueous suspension, prepared at a solid loading of 8 vol%, was dispersed by ball milling for about 15 h. Few drops of diluted hydrochloric acid were added to the suspension, in order to decrease the starting pH (around 6) to 3, and this value was monitored and kept constant all over the process. Zirconia spheres (Tosoh Corporation, 2.0 mm in diameter, weight ratio of 1:10 with respect to the powder) were selected as milling media since they exhibit high crushing strength and wear resistance [19]. The particle size distribution was determined by

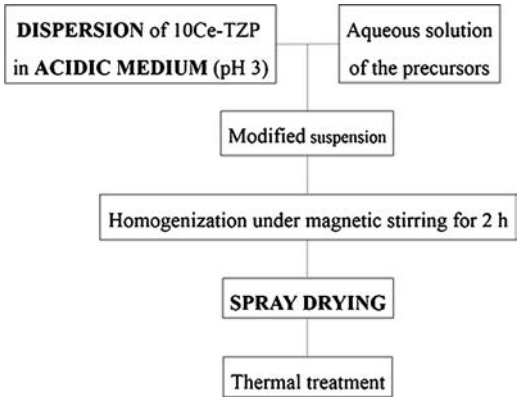

Fig. 1. Flow-chart of the adopted procedure for the elaboration of the composite powders. Bold character denotes the most critical steps in the process.

using laser-granulometry (Fristch Analysette 22) whereas the possible release of ceria from the stabilized zirconia powders, due to the acidic pH, was investigated by ICP-AES analysis (Optima 2100, Perkin Elmer). The nitrates were then dissolved in distilled water, until clear solutions were obtained. The nitrate solutions were drop-wise added to the dispersed zirconia slurry; the modified suspension was kept under magnetic stirring for 2 h to assure homogeneity and finally spray-dried.

On the basis of previous experiences [16,18], the doped powders were pre-treated at 600 °C for 1 h at the heating rate of 10 °C/min with the aim of inducing the decomposition of the by-products. In addition, a second pre-treatment was carried out in the 900–1450 °C temperature range to induce the crystallization of the second phases on the zirconia particle surface. In order to investigate the phase evolution, XRD diffraction analyses were performed (Philips PW 1710 with a Cu K_α anticathode, 10–70° range in 2θ, step size of 0.05° and a time for step of 5 s). The Toraya equation [20] was used to determine the monoclinic volume fraction (V_m).

2.3. Forming and sintering

Composite powders, calcined at 1150 °C for 30 min, as well as pure 10Ce-TZP powder were used to prepare slip cast green bodies. Aqueous suspensions were prepared at a solid loading of 26 vol%, with 3 wt% (as respect to the powder weight) of a commercial dispersant (Duramax D-3005). The suspensions were dispersed by ball-milling (zirconia milling spheres were used) for 30 h. The evolution of the particle size distribution within the dispersion time was determined by laser granulometry.

The slips were de-aired by keeping them under vacuum for few minutes and then cast into pure alumina, porous moulds. Green bodies were dried into a humidity-controlled chamber for about 1 week. Debinding was carried out at 600 °C for 1 h (heating and cooling rate of 2 °C/min). The densification behaviour was investigated by dilatometric analyses (Netzsch 402E), carried out up to 1500 °C for 1 h. Heating and cooling rate of 5 °C/min were used [16]. On the ground of these results, materials were pressureless sintered in the range 1250–1650 °C, for different dwell times (1–2 h).

2.4. Characterization

The green and fired densities were evaluated by mass-geometric measurements and Archimedes method, respectively, and referred to the materials theoretical density (TD), calculated by the rule of mixtures for composite systems (values of 6.19, 5.82, 3.99, 4.02 and 4.24 g/cm^3 for tetragonal and monoclinic ZrO_2, α-Al_2O_3, $SrAl_{12}O_{19}$ and $CeMgAl_{11}O_{19}$ were respectively used). The microstructures were observed by means of Field Emission Scanning Electron Microscopy (FESEM Hitachi S4000) on polished and thermally etched specimens. The mean grain sizes of matrix and second phases were determined by image analysis (Scandium Soft imaging system software). In addition, high-resolution Transmission Electron Microscopy (HRTEM JOEL 2010 F), equipped with a nanoprobe for EDX analyses and X-rays mapping, was carried out. Selected Area Diffraction (SAED) and Fast Fourier Transform (FFT) of the HRTEM images from DigitalMicrograph^{TM} software were used to index the crystalline phases. Finally, in order to investigate the capability of composite materials to undergo a stress-induced *t–m* phase transformation, Vickers indentations (Testwell Vickers Indenter FV-700, France) were performed. The extension of the transformed area around Vickers indentations was evaluated by means of ImageJ program. The role of the applied loads on the transformability was investigated by applying three different loads – 5, 10, 30 kg_f – for 10 s. Five indentations for each load were performed on surfaces polished down to 1 μm with the aim of obtaining an average value of the transformed area.

3. Results and discussion

3.1. Elaboration and characterization of the composite powders

Ball-milling of 10Ce-TZP powder was carried out for 15 h, under acid conditions (pH of 3). In fact, according to the Z-potential curve of ceria-stabilized zirconia given in literature data [21], the best dispersibility conditions – far from the isoelectric point – can be achieved either under acid and basic medium. Therefore, for the selection of the most suitable suspension pH, we have considered the precipitation curves of the metal ions, precursors of the second phases. Experimentally, we determined that the precipitation of aluminium, magnesium and cerium hydroxide occurs at pH of 4.5, 10.5 and 7.5, respectively. On the contrary, the precipitation of strontium hydroxide did not occur even at basic pH values (>14). According to these data, we decided to carry out the dispersion under acid conditions, favouring a close mixing between the nanometric zirconia particles and the dissolved metal ions. The acidic dispersion did not induce any solubilization of cerium from the zirconia lattice, as verified by ICP-AES analysis. It was successful to halve the starting agglomerate size, from the average value of 1.1 to 0.5 μm. This value was considered as a threshold, since it did not further decrease, even after additional milling time.

A micrograph of the dispersed powder is depicted in Fig. 2, showing agglomerates of about 200–800 nm in size, in which primary particles of about 50–100 nm can be clearly identified.

A fast drying, carried out by atomization, was required for (i) avoiding the ions segregation and (ii) assuring homogeneous

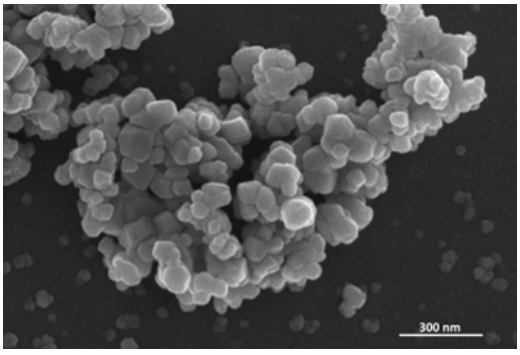

Fig. 2. FESEM micrograph of the dispersed 10Ce-TZP powder.

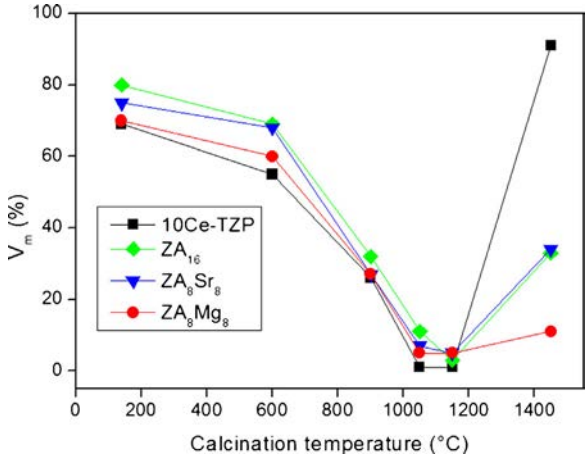

Fig. 3. Evolution of the monoclinic volume fraction (V_m) as a function of the calcination temperature for 10Ce-TZP (black square), ZA_{16} (green diamond), ZA_8Sr_8 (blue triangle) and ZA_8Mg_8 (red circle) powders. (For interpretation of the references to color in this figure legend, the reader is referred to the web version of the article.)

coating on the zirconia particles and distribution of the second-phases in the final composites, as previously demonstrated for alumina-based materials [18].

In Fig. 3, the evolution of the monoclinic volume fraction (V_m) of 10Ce-TZP, ZA_{16}, ZA_8Sr_8 and ZA_8Mg_8 powders as a function of the thermal treatments is depicted. We can see that all as-prepared powders are characterized by high V_m values, in the range 70–80 vol%. In addition, we can observe a clear influence of the thermal treatment on V_m: independently from the composition, V_m progressively decreased by increasing the calcination temperature, reaching the lowest values (3–5 vol%) at 1050–1150 °C. Since the same trend was observed in both 10Ce-TZP and in the composite powders, we can suppose a negligible role of the second phases in decreasing V_m. In the case of pure 10Ce-TZP, the behaviour can be easily justified on the ground of the ceria-zirconia phase diagram [1]. The increased (meta)stabilization of the *t*-phase by increasing the calcination temperature can be also imputed to an increasing effect of ceria inside the zirconia lattice, being the diffusion of the cerium oxide promoted by the higher temperature treatments [22]. From Fig. 3, we can also see that V_m significantly increased at 1450 °C, for all the investigated materials. In such conditions, we can suppose that the size of both zirconia particles and agglomerates increases, thus leading to an increase of the amount of monoclinic zirconia. Nevertheless, here a clear role of the second phases can be stated. In fact, pure 10Ce-TZP showed the highest amount of V_m (91 vol%), whereas the second-phases partially hindered the *t–m* transformation, giving rise to lower values (V_m in the range 10–34%). The lowest V_m was observed in ZA_8Mg_8, thus suggesting a certain role of cerium added during synthesis in stabilizing the *t*-ZrO_2 phase. This issue will be discussed later.

3.2. Processing and sintering

All composite powders were treated at 1150 °C for 30 min, since they are characterized by a low volume fraction of monoclinic zirconia (see Fig. 3). A strong decrease of the agglomerate size was observed after about 30 h of ball milling, whatever the composition of the thermally treated powders. The diameter corresponding to 10, 50 and 90% of the cumulative size distribution (d_{10}, d_{50} and d_{90}, respectively) of ZA_{16}, ZA_8Sr_8 and ZA_8Mg_8 are reported in Table 1. After ball milling, mean diameters (d_{50}) of 0.5 μm and d_{90} values lower than 1 μm were observed.

Table 1
Diameters (d_{10}, d_{50} and d_{90}) corresponding to 10, 50 and 90% of the cumulative size distribution (by volume) before and after ball-milling of ZA_{16}, ZA_8Sr_8 and ZA_8Mg_8 powders.

	d_{10} (μm)	d_{50} (μm)	d_{90} (μm)
ZA_{16}	7.0	74.0	252.0
ZA_{16} 30 h – ball milled	0.3	0.5	1.0
ZA_8Sr_8	11.0	42.0	255.0
ZA_8Sr_8 30 h – ball milled	n.d.[a]	0.5	0.9
ZA_8Mg_8	6.0	28.0	211.0
ZA_8Mg_8 30 h – ball milled	n.d.[a]	0.5	1.0

[a] Below the instrumental limit (<0.31 μm).

The sintering behaviour of pure 10Ce-TZP was compared to that of biphasic and triphasic materials. All samples were sintered at 1500 °C for 1 h. Fig. 4 collects the densification (left) and derivative (right) curves (during the heating step) of 10Ce-TZP (black line), ZA_{16} (green line), ZA_8Sr_8 (blue line) and ZA_8Mg_8 (red line) materials. The corresponding main data from dilatometric analyses as well as green and fired densities are collected in Table 2.

The slip cast green bodies from the composite powders had a similar density of about 48–49%TD. A higher green density (~56%TD) was observed for 10Ce-TZP materials. After sintering, all materials reached full densification (99.9%TD). Derivative curves (Fig. 4b) allow to evidence that the second-phase dopants induce an increase of the onset sintering temperature (T_{onset}, data in Table 2): it was about 1025 °C for pure 10Ce-TZP, 1081 °C for ZA_8Mg_8 and even higher, 1125 and 1160 °C, respectively, for ZA_{16} and ZA_8Sr_8 materials. Moreover, in the case of 10Ce-TZP sample, a single inflection point at about 1183 °C was detected, imputed to the temperature at which the maximum sintering rate occurs (referred to as T_{max}). For what concerns composite materials two inflection points were observed. The former, located in the range 1208–1255 °C (referred to as $T_{transformation}$), can be reasonably imputed to the crystallization of second phases from transition phases. In order to explain the crystallization phenomena involved in these composites, we refer to the work of Douy et al. [23]. Precisely, for ZA_8Sr_8 powder, it is supposed that alumina crystallizes into γ-Al_2O_3 phase at about 950 °C, transforming to the high temperature phases (α-Al_2O_3 and $SrAl_{12}O_{19}$) at about 1200 °C.

The latter, in the range 1315–1397 °C, can be again imputed to the temperature of maximum sintering rate. The comparison of such values with the 10Ce-TZP data highlights the role of second-phases in delaying densification of zirconia. More in details, α-alumina phase induced the highest delay and the magnesium aluminate the lowest, being T_{max} about 1315, 1377 and 1397 °C for ZA_8Mg_8, ZA_8Sr_8 and ZA_{16}, respectively. Being

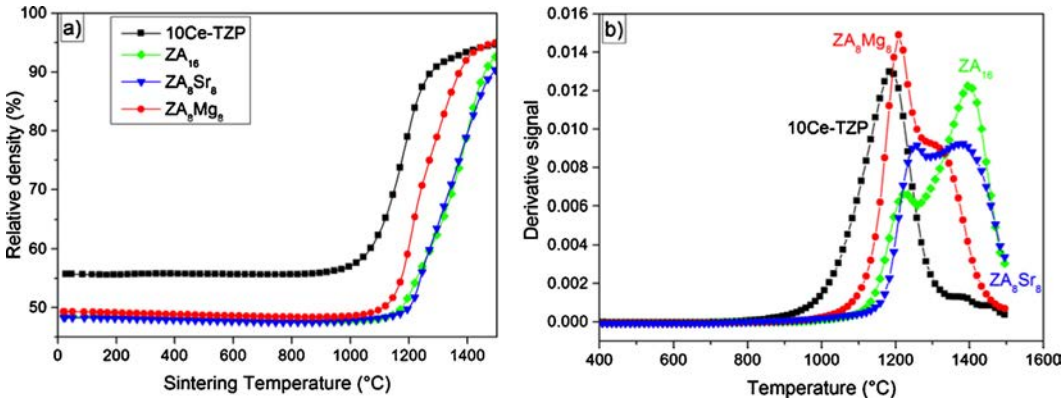

Fig. 4. Densification (left) and derivative (right) curves of 10Ce-TZP (black square), ZA_{16} (green diamond), ZA_8Sr_8 (blue triangle) and ZA_8Mg_8 (red circle) materials, all sintered at 1500 °C for 1 h. (For interpretation of the references to color in this figure legend, the reader is referred to the web version of the article.)

Table 2
Green density, fired density and main data from the dilatometric analysis of 10Ce-TZP, ZA_{16}, ZA_8Sr_8 and ZA_8Mg_8 sintered at 1500 °C for 1 h.

	Green density (%TD)	Fired density (%TD)	T_{onset} (°C)	$T_{transformation}$ (°C)	T_{max} (°C)
10Ce-TZP	55.7	>99.9	1025	–	1183
ZA_{16}	48.5	99.9	1125	1224	1397
ZA_8Sr_8	48.3	99.9	1160	1255	1377
ZA_8Mg_8	49.3	>99.9	1081	1208	1315

well-known the role of magnesia as sintering aid for alumina, we can suppose a similar role also in this complex composite system.

3.3. Characterization of sintered materials

In order to deepen the role of second phases on the fired density and phase composition, further sintering cycles were performed in the range 1250–1650 °C, for different dwell times (1–2 h). The evolution of the fired density and monoclinic volume fraction (evaluated on the sintered surface) as a function of the sintering temperature is depicted in Fig. 5a–d for 10Ce-TZP, ZA_{16}, ZA_8Sr_8 and ZA_8Mg_8, respectively. 10Ce-TZP material reached full densification (99.9%TD) at very low temperature (1250 °C), giving rise to a material prevalently made of *t*-ZrO_2 phase (V_m equal to 4%). However, this value rose to about 17% after a mild polishing of the surface, producing a severe pull-out of the surface grains, as described in the following. All other sintering cycles, carried out at higher temperatures, gave rise to fully dense 10Ce-TZP materials but characterized by a high amount of monoclinic phase, in the range 76–93 vol%. This result is in agreement with the densification curves, showing a T_{max} of 1183 °C. On the contrary, in order to reach full densification, but low V_m, both ZA_{16} and ZA_8Sr_8 composites required a higher sintering temperature equal to 1450 °C. In fact, as shown in Fig. 5b and c, sintering cycles at 1350 °C and 1400 °C were not sufficient to induce full densification, whereas higher temperatures gave rise to significant amounts of monoclinic phase. Finally, ZA_8Mg_8 materials reached full density (99.9%TD) in the entire investigated temperature range (1350–1650 °C), in agreement with the T_{max} revealed by dilatometric analyses. However, it was possible to retain a low amount of monoclinic phase only up to 1400 °C; for higher sintering temperature, V_m quickly rose up to 80 vol%.

On the ground of the above data and results from dilatometry, optimal sintering cycles were selected for each composition, with the aim of obtaining simultaneously full densification and low V_m values. Precisely, 1250 °C for 2 h for 10Ce-TZP and 1350 °C for 2 h for ZA_8Mg_8 were chosen, whereas 1450 °C for 1 h was selected for both ZA_8Sr_8 and ZA_{16} materials. Fig. 6 shows the XRD patterns of the materials sintered following the optimal conditions: in addition to monoclinic (ICDD no. 74-0815) and tetragonal (ICDD no. 82-1398) zirconia phase, XRD spectrum of ZA_{16} showed also the presence of α-Al_2O_3 phase (ICDD no. 46-1212). In the ZA_8Sr_8 sintered sample we can also observe peaks imputable to the $SrAl_{12}O_{19}$ phase (ICDD no. 80-1195), even if their intensity is very low compared to those related to zirconia phase. In the case of ZA_8Mg_8 sintered at 1350 °C for 2 h, we can see that, beside zirconia, only α-Al_2O_3 phase can be observed. The intensity of $CeMgAl_{11}O_{19}$ phase was probably lower than the instrumental detection limit, and thus was not detected. In fact, it should be mentioned that the intensity of the diffraction peaks is related to the amount of the phase, the crystallization degree and to the Z-number.

Microstructural images of the materials sintered following the above optimal conditions are reported in Fig. 7. In order to appreciate the evolution of the microstructure with temperature, also FESEM images of 10Ce-TZP and ZA_8Mg_8 sintered respectively at 1450 and 1400 °C for 1 h, are displayed. The corresponding microstructural features in terms of zirconia and alumina grains size, length and aspect ratio of aluminate grains are collected in Table 3. In 10Ce-TZP material sintered at 1250 °C for 2 h (Fig. 7a) a sever pull-out of surface grains can be easily observed, probably due to surface polishing and

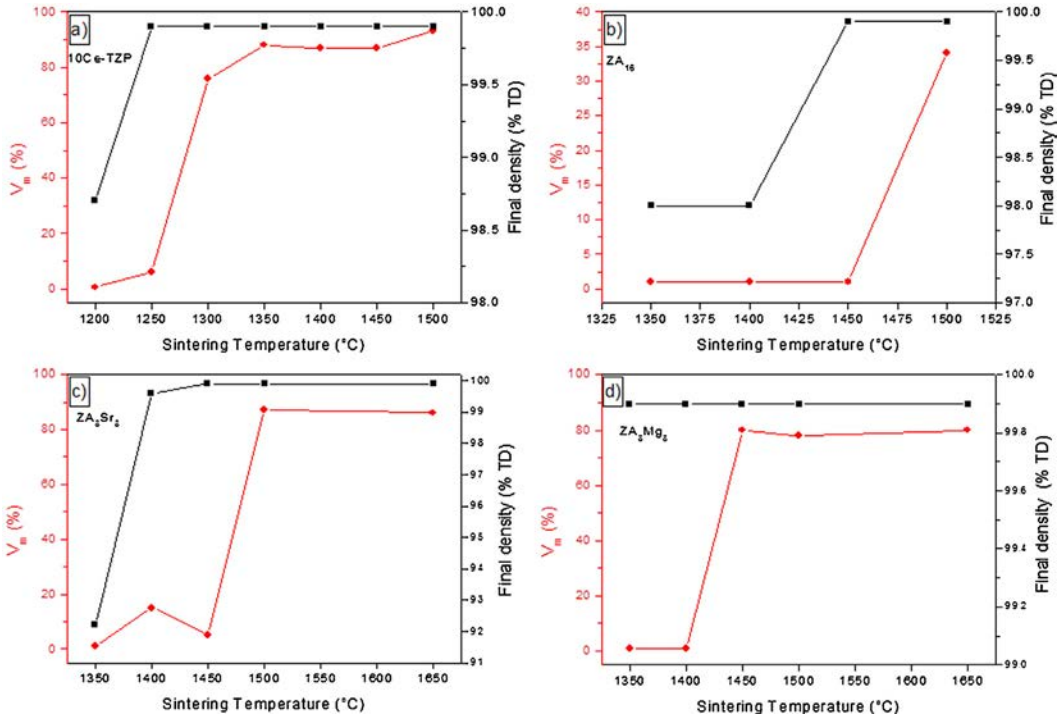

Fig. 5. Monoclinic volume fraction (V_m) and final density (%TD) as a function of the sintering temperature for: 10Ce-TZP (a), ZA_{16} (b), ZA_8Sr_8 (c), and ZA_8Mg_8 (d) materials.

Table 3
Microstructural features (zirconia and alumina grains size, length and aspect ratio of aluminate grains) of the investigated materials.

	ZrO_2 mean size (μm)	Al_2O_3 mean size (μm)	Aluminate mean length (μm); aspect ratio
10Ce-TZP/1250 °C – 2 h	0.4 ± 0.1	–	–
10Ce-TZP/1450 °C – 1 h	1.7 ± 0.6	–	–
ZA_{16}/1450 °C – 1 h	0.5 ± 0.1	0.3 ± 0.1	–
ZA_8Sr_8/1450 °C – 1 h	0.6 ± 0.2	0.3 ± 0.1	0.6 ± 0.2 a.r. 6 ± 2
ZA_8Mg_8/1350 °C – 2 h	0.4 ± 0.3	0.3 ± 0.1	2 ± 1 a.r. 6 ± 3
ZA_8Mg_8/1400 °C – 1 h	0.8 ± 0.3	0.3 ± 0.1	4 ± 2 a.r. 9 ± 3

consequently phase transformation of a relevant fraction of t-ZrO_2 grains, as stated by XRD. The average zirconia grain size was about 400 nm, as can be observed in the higher magnification image inset to the figure. As expected, by increasing the sintering temperature, the microstructure became coarser: the grain size rose to 1.7 μm at 1450 °C (Fig. 7b).

More interesting, FESEM observations of ZA_{16} sintered at 1450 °C for 1 h (Fig. 7c) showed a fully homogeneous distribution of alumina particles (dark, equiaxial grains) inside the zirconia matrix (brighter grains). Alumina particles were mainly located in inter-granular positions but a fraction of them was also observed inside zirconia grains (intra-granular positions). The micrograph of ZA_8Sr_8 sintered at 1450 °C for 1 h (Fig. 7d) revealed a more complex composite microstructure characterized by the presence of both rounded (α-Al_2O_3 phase) and elongated ($SrAl_{12}O_{19}$ phase) grains, both well-dispersed inside the matrix. By image analysis, an average particle size of 0.6 ± 0.2 μm and of 0.3 ± 0.1 μm for zirconia and alumina

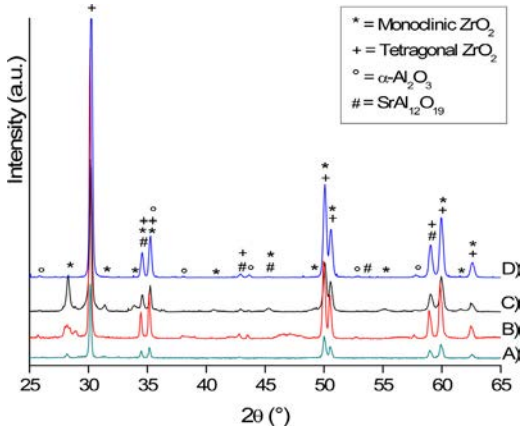

Fig. 6. XRD spectra of sintered materials: (A) 10Ce-TZP/1250 °C – 2 h, (B) ZA_{16}/1450 °C – 1 h, (C) ZA_8Sr_8/1450 °C – 1 h and (D) ZA_8Mg_8/1350 °C – 2 h.

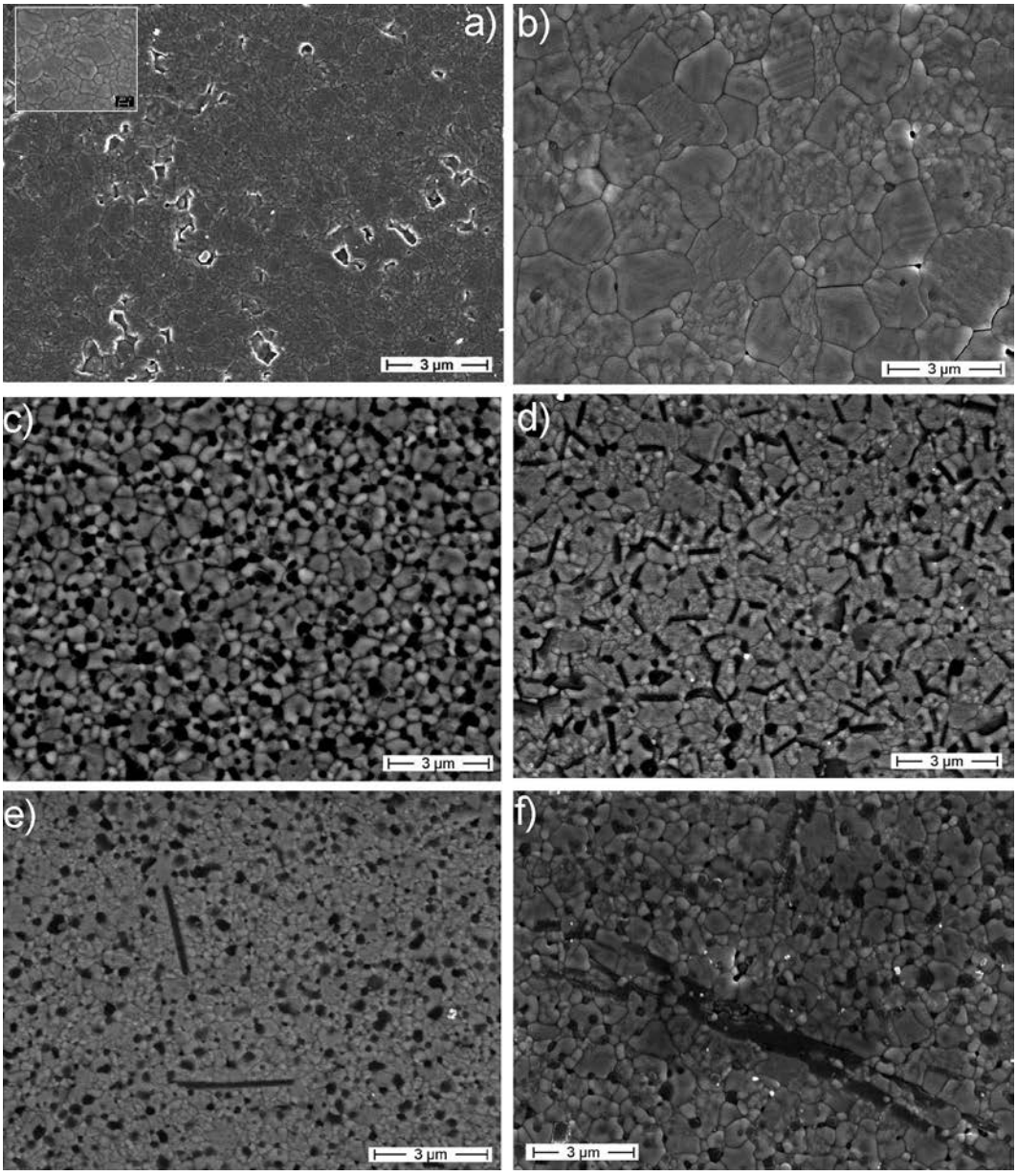

Fig. 7. FESEM micrographs of sintered materials: 10Ce-TZP/1250 °C – 2 h (a); 10Ce-TZP/1450 °C – 1 h (b); ZA_{16}/1450 °C – 1 h (c); ZA_8Sr_8/1450 °C – 1 h (d); ZA_8Mg_8/1350 °C – 2 h (e) and ZA_8Mg_8/1400 °C – 1 h (f).

grains, respectively, were determined. The strontium hexaluminate grains were characterized by mean length of 0.6 ± 0.2 μm and aspect ratio (a.r.) of 5 ± 2. The comparison between the zirconia grain size in 10Ce-TZP, ZA_{16} and ZA_8Sr_8, all sintered at 1450 °C for 1 h (see Fig. 7b–d) highlights the ability of the second phase particles to exert an effective *pinning* on zirconia grain boundaries, thus significantly refining the matrix grain size. Such result was achieved thanks to the optimal distribution of the second phase inside the composite materials. In Fig. 7e, the microstructure of ZA_8Mg_8 sintered at 1350 °C for 2 h is reported. Although XRD analyses revealed only the presence of alumina as second phase (see Fig. 6), FESEM observations allowed observing darker elongated grains, imputed to the $CeMgAl_{11}O_{19}$ phase. The microstructure was homogeneous and fine, similar to that observed for the previous composites.

All composite materials were also observed after submitting them to the same temperature increment (of 50 °C) from their best sintering cycle: ZA_{16} and ZA_8Sr_8 were sintered at 1500 °C for 1 h, ZA_8Mg_8 at 1400 °C for 1 h. This temperature increment did not produce any remarkable effect on the microstructure of ZA_{16} and ZA_8Sr_8 composites: the materials were still very homogeneous and retained their very fine grain size. On the opposite, important differences were observed in ZA_8Mg_8, passing from 1350 °C/2 h to 1400 °C/1 h (Fig. 7e and f). In this last composite, a bimodal distribution of zirconia grain size can be observed. In fact, some large zirconia grains (of some microns in length), near smaller zirconia particles, of about 600 nm in size can be observed. Large zirconia grains are mainly located close to elongated grains. The zirconia grain size was about 0.8 μm, with elongated grains of about 4 μm in length. In addition, a

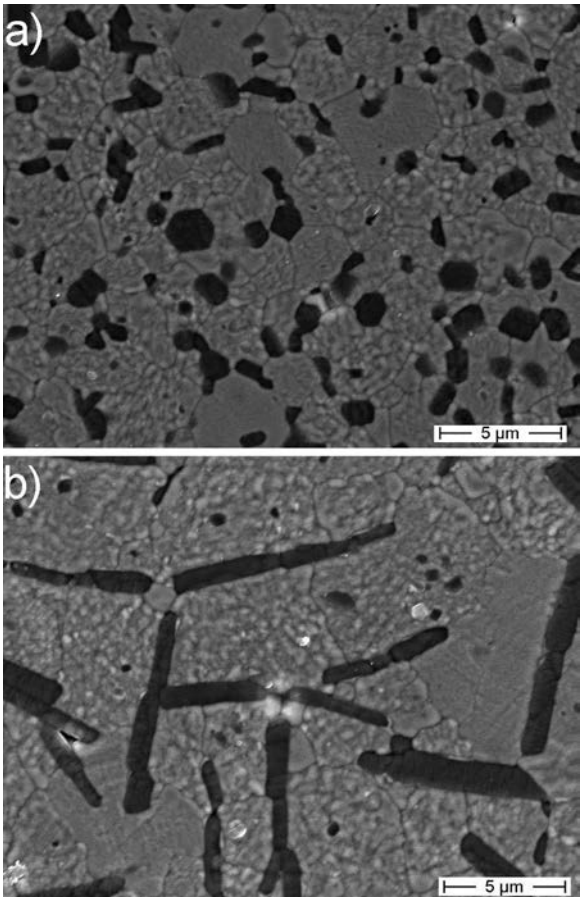

Fig. 8. FESEM micrographs, at different magnifications, of ZA_8Sr_8 (a) and ZA_8Mg_8 (b) sintered at 1650 °C for 1 h.

strong difference in the morphology of the elongated grains can be observed by comparing FESEM micrographs of ZA_8Mg_8 sintered at 1350 and 1400 °C. Few isolated, elongated grains can be observed in the former case. On the contrary, a bigger amount of complex elongated and platelet-like grains can be noticed in the latter case. In any case, the morphology the Sr-rich elongated grains was quite different from those containing Ce/Mg, as can be stated by comparing the images in Fig. 7c and e/f.

In order to deepen if further high-temperature treatments could enhance or annihilate such microstructural differences, ZA_8Sr_8 and ZA_8Mg_8 composites were sintered at 1650 °C for 1 h. Their microstructures are compared in Fig. 8. Besides the expected increase of the grains size, we can appreciate very different microstructural features. ZA_8Sr_8 consists now in a micronic zirconia matrix (mean size of about 2.6 μm), containing platelet-like grains. Few elongated morphologies can now be observed, characterized by length of about 1.5 μm and a.r. of 2–2.5. The overall coarsened microstructure accounts for the very high monoclinic volume fraction (0.86) observed in this material (see Fig. 5c). On the opposite, the elongated morphology was maintained in ZA_8Mg_8, showing large zirconia grains (up to 5 μm), with well-developed elongated grains of about 3.5 μm in length and a.r. of about 4.

A deepening of the microstructure and composition of the triphasic composites, and particularly of the elongated morphologies was carried out by HRTEM. The analyses were performed on ZA_8Sr_8 and ZA_8Mg_8 sintered at 1450 °C/1 h and 1350 °C/2 h, respectively. The corresponding micrographs and associated EDX maps are reported in Figs. 9 and 10: we can observe that aluminium is located in both rounded and elongated darker grains. Strontium and magnesium are revealed only in the elongated grains of ZA_8Sr_8 and ZA_8Mg_8, respectively. Finally, in the case of ZA_8Sr_8, cerium was exclusively detected in the zirconia grains (brighter grains) while in the case of ZA_8Mg_8 it was also present in the elongated grains, strengthening the formation of the desired magnesium aluminate $CeMgAl_{11}O_{19}$ phase. The mean composition (at%) of the kind of grains referred to as A, B and C in Figs. 9 and 10 is reported in the table associated to the same figures. A good matching between the experimental values and the nominal ones was found in both samples, thus suggesting the ability of the adopted elaboration process in tailoring the chemical composition even of complex multi-cation phases. Precisely, concerning the elongated grains, the atomic Sr:Al ratio of 5.1:84.3 ($Sr_{0.7}Al_{12}O_x$) was close to the ratio in $SrAl_{12}O_{19}$. Whereas, Ce:Mg:Al ratio of 8.6:6.1:84.1 revealed the phase composition of $Ce_{1.1}Mg_{0.8}Al_{11}O_x$. However, a certain discrepancy with respect to the nominal composition is observed since EDX measurements obtained in a TEM are bound by some uncertainties due to two main effects. The first one is the limited accuracy resulting of the more or less intense X-rays flow (governed by the acquisition time and foil thickness). Typically, a result of 50 at% has a standard deviation around 1 at%. The second one is attributed to a well-known artefact due to backscattered electrons out of the beam. The consequence is an X-ray parasite signal when an analysis is made on a small particle embedded inside a matrix. In our case, a small Zr-signal is observed during an alumina particle analysis and reciprocally in the case of a high density of particles. So, here, it is convenient to exclude the presence of Zr inside alumina and Al inside zirconia. Moreover, although the absorption corrections are applied, the oxygen content results are not enough secure.

Finally, it should be noticed that a weak diffusion of cerium inside zirconia grains was revealed in ZA_8Mg_8, being its concentration of 11.4 at% rather than 10 at%, as in the case of ZA_8Sr_8 (Fig. 9). This can be explained keeping in mind that during the elaboration process of ZA_8Mg_8 a proper amount of cerium nitrate was added with the aim of developing the $CeMgAl_{11}O_{19}$ phase. Thus, although some uncertainty of the EDX measurements, as previously reported, we can suppose a certain cerium diffusion inside zirconia grains promoted by high temperatures. In both ZA_8Sr_8 and ZA_8Mg_8, FFT analyses (not shown) allowed to correlate alumina grains with the crystallography of α-Al_2O_3 phase (ICDD no. 46–1212). At the same time, FFT from HRTEM of zirconia grains (not shown) were correlated to tetragonal-ZrO_2 (ICDD no.82-1398) phase. FFT from HRTEM micrographs of an aluminate grain of ZA_8Sr_8 and ZA_8Mg_8 are depicted in Fig. 11a and b, respectively. Experimental lattice distances compared to the theoretical ones (see table associated to the same figure) revealed in both cases a good agreement with $SrAl_{12}O_{19}$ (ICDD no 80-1195) and $CeMgAl_{11}O_{19}$ (ICDD no. 26-0872) phase.

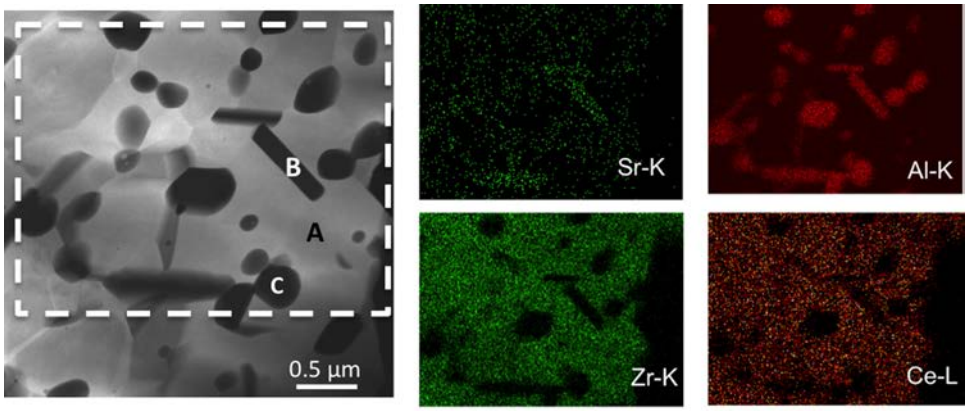

	Zr (at%)	Ce (at%)	Al (at%)	Sr (at%)	Composition
Kind A (5 particles)	88.5	9.1	2.1	0.2	$Zr_1Ce_{0.103}O_x$
Kind B (7 particles)	9.2	1.4	84.3	5.1	$Sr_{0.72}Al_{12}O_x$
Kind C (7 particles)	8.5	< 0.1	89.8	0.1	Al_2O_3

Fig. 9. TEM image (on the left) and EDX maps (on the right) of ZA_8Sr_8/1450 °C – 1 h. A–C letters indicate each kind of internal compounds: A for Zr-based matrice, B for Sr-aluminate and C for pure alumina. Below, the table gives the mean chemical composition for each kind (white dot in grain B illustrates the electron beam impact).

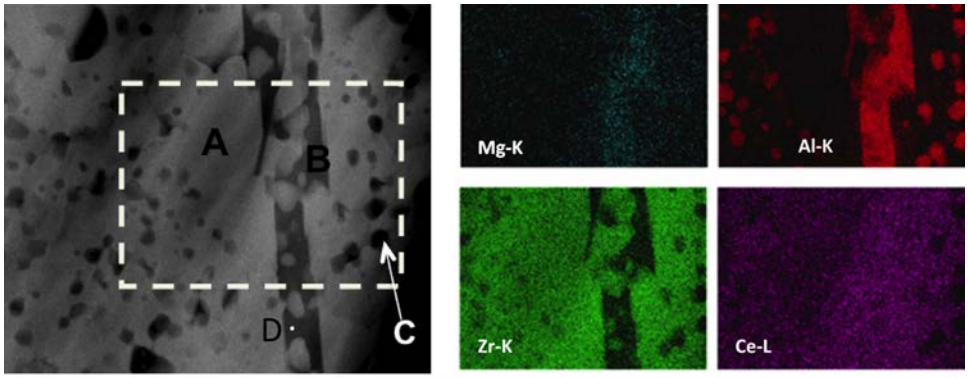

	Zr (at%)	Ce (at%)	Al (at%)	Mg (at%)	Composition
Kind A (14 particles)	88.6	11.4	0	0	$Zr_1Ce_{0.13}O_x$
Kind B (4 particles)	1.1	8.6	84.1	6.1	$Ce_{1.1}Mg_{0.8}Al_{11}O_x$
Kind C (4 particles)	0.9	0.2	99	0	Al_2O_3

Fig. 10. TEM image (on the left) and EDX maps (on the right) of ZA_8Mg_8/1350 °C – 2 h. A–C letters indicate each kind of internal compounds: A for Zr-based matrice, B for (Ce,Mg)-aluminate and C for pure alumina. Below, the table gives the mean chemical composition for each kind (white dot D illustrates the electron beam impact).

Preliminary results regarding the transformability of composite materials were obtained by performing Vickers indentations. The size of the transformed area around each indentation as a function of the applied load (5 – 10 – 30 kg_f) for ZA_{16}/1450 °C – 1 h, ZA_8Sr_8/1450 °C – 1 h and ZA_8Mg_8/1350 °C – 2 h is reported in Fig. 12. Optical images of some indents of ZA_{16} sintered at 1450 °C/1 h and ZA_8Mg_8 sintered at 1350 °C/2 h materials are also compared in the same figure. The zone in which the tetragonal to monoclinic transformation occurred, producing a volume expansion, can be clearly associated to the brighter zone observed around the indentation. ZA_{16} and ZA_8Sr_8 (not illustrated) showed a wider transformed zone compared to ZA_8Mg_8, revealing a higher transformability. Moreover, different morphologies of the transformed zone can be recognized: a large number of deformation branches that propagate radially from the imprints were observed on ZA_{16} surfaces, highlighting the autocatalytic nature of the tetragonal to monoclinic transformation [24]. On the opposite, smaller and rounded-shape transformed zones were observed on ZA_8Mg_8 surfaces. The amount of tetragonal phase able to transform into monoclinic phase is directly related to the applied load. Higher the indenter load, higher the size of the transformed zone, whatever the

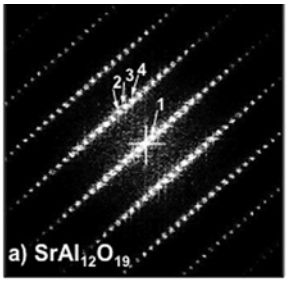

Spot	d_{exp} (nm)	$d_{SrAl12O19}$	hkl	Deg. to spot 1	Deg. $SrAl_{12}O_{19}$
1	2.22	2.20	{0001}	0°	0°
2	0.483	0.482	{1-100}	90°	90°
3	0.476	0.471	{1-101}	78°	77.6°
4	0.446	0.442	{1-102}	66°	66.3°

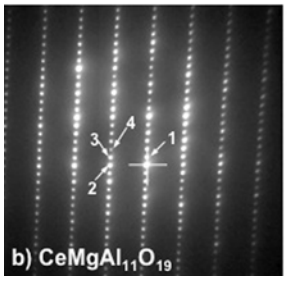

Spot	d_{exp} (nm)	$d_{CeMgAl11O19}$	hkl	Deg. to spot 1	Deg. $CeMgAl_{11}O_{19}$
1	2.21	2.199	{0001}	0°	0°
2	0.488	0.485	{10-10}	93°	90°
3	0.480	0.476	{10-11}	80°	77.5°
4	0.455	0.441	{10-12}	69°	66.2°

Fig. 11. SAED patterns and FFT analyses of a $SrAl_{12}O_{19}$ grain in zone axis [0 1 0] (a) and $CeMgAl_{11}O_{19}$ grain in zone axis [0 1 0] in the region labelled D in Fig. 10 where the EDX composition was found as $Ce_{1.2}Mg_{0.7}Al_{11}O_{21}$ (b).

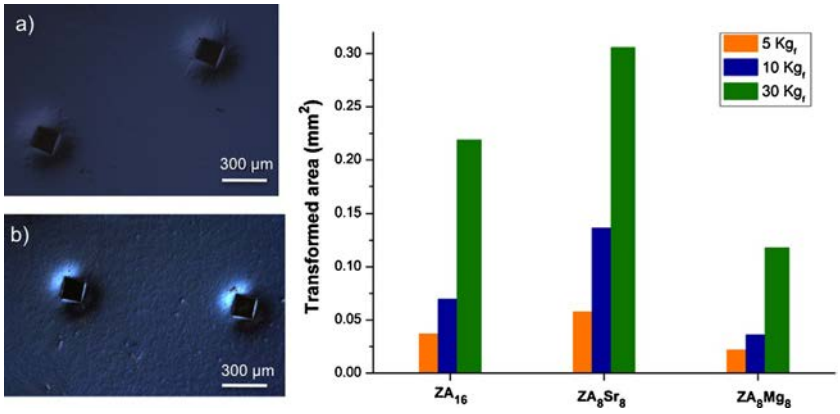

Fig. 12. On the right: optical images of 30 kg_f Vickers indentations of ZA_{16}/1450 °C – 1 h (a) and ZA_8Mg_8/1350 °C – 2 h (b). On the left: transformed area around indentation as a function of the indenter load for ZA_{16}/1450 °C – 1 h, ZA_8Sr_8/1450 °C – 1 h and ZA_8Mg_8/1350 °C – 2 h.

composition. Nevertheless, the influence of the amount and type of second phases on the materials transformability can be clearly observed. The comparison between ZA_{16} and ZA_8Sr_8 highlights the higher transformability of the latter one, since it is characterized by a lower amount of alumina phase. In fact, it is well known that the tetragonal to monoclinic transformation is hindered by a second phase, such as alumina, which is stiffer than zirconia [1]. Although ZA_8Sr_8 and ZA_8Mg_8 are characterized by the same amount of alumina phase, a strong difference in transformability can be observed. The lowest transformability of ZA_8Mg_8 is imputable to the higher amount of ceria inside zirconia grains revealed by TEM analyses. Since zirconia grains in ZA_8Mg_8 are stabilized by about 11 mol% of ceria, instead of 10 mol% present in both ZA_{16} and ZA_8Sr_8, they showed a lower transformability. Thus, we can assert that both the nature of the second phase as well as the stabilization degree of zirconia grains strongly affect the transformability.

4. Conclusions

Sintering of Ce-TZP materials is a complex exercise and should be carefully controlled in order to produce fully dense, fine materials but still able to give rise to the tetragonal-to-monoclinic toughening transformation under an applied stress. With this in mind, we have developed three different types of 10Ce-TZP-based composites with the aim of investigating the role of second phases on the sintering behaviour and zirconia transformability. Equiaxial α-Al_2O_3 and two kinds of elongated particles, precisely $SrAl_{12}O_{19}$ and $CeMgAl_{11}O_{19}$, were selected as second-phases. Composite powders were developed through a surface coating route, which allowed a precise tailoring of phase composition, as revealed by HRTEM analyses. A limited cerium diffusion inside zirconia grains, promoted by high temperatures, was found out when $CeMgAl_{11}O_{19}$ was added to zirconia matrix, thus affecting its stabilization.

Second-phases led to a delay of zirconia densification: the most relevant one was induced by the presence of the alumina phase, with respect to monolithic 10Ce-TZP. The optimal sintering cycle needed to reach full densification and low monoclinic fraction strongly depends on the nature of the second-phases. Such conditions were fulfilled at low sintering temperatures (1350–1400 °C) in the system containing the $CeMgAl_{11}O_{19}$ phase, whereas a sintering temperature of 1450 °C was required in the presence of Al_2O_3 and $SrAl_{12}O_{19}$. Microstructural features were tailored by both phase composition and sintering parameters: highly homogeneous and fine microstructures were observed due to the effective *pinning* exerted by the second-phases on the zirconia grain boundaries. Strong differences in morphologic features (length and aspect ratio) of the elongated grains between $CeMgAl_{11}O_{19}$ and $SrAl_{12}O_{19}$ were revealed by FESEM. Such differences raised by increasing the sintering temperature. Strong differences in the size and morphology of transformed area among the composites were revealed by Vickers indentations. All composite presented a good stress-induced transformability, but the lowest efficiency of *t–m* transformation was observed in the three-phase system containing Al_2O_3 and $CeMgAl_{11}O_{19}$. As a whole, we have here demonstrated that a careful tailoring of phase composition (for both zirconia and second phases) and microstructure can lead to materials characterized by very fine microstructure and significant transformability. This suggests interesting mechanical properties (in terms of both strength and fracture toughness) of these new composites, as we will describe in future works.

Acknowledgements

The research leading to these results has been performed within the LONGLIFE project (www.longlife-project.eu) and received funding from the European Community's Seventh Framework Programme (FP7/2007-2013) under grant agreement no. 280741.

The authors would like to acknowledge the CLYM (Centre Lyonnais de Microscopie (http://www.clym.fr) for the access of the JEOL 2010F.

References

[1] Chevalier J, Gremillard L, Virkar AV, Clarke DR. The tetragonal–monoclinic transformation in zirconia: lesson learned and future trends. J Am Ceram Soc 2009;92:1901–20.
[2] Cattani-Lorente M, Scherrer SS, Ammann P, Jobin M, Wiskott A. Low temperature degradation of a Y-TZP dental ceramic. Acta Biomater 2011;7:858–65.
[3] Chevalier J, Gremillard L. Ceramics for medical applications: a picture for the next 20 years. J Eur Ceram Soc 2009;29:1245–55.
[4] Sergo V, Schmid C, Meriani S, Evans AG. Mechanically induced zone darkening of alumina/ceria-stabilized zirconia composites. J Am Ceram Soc 1994;77:2971–6.
[5] Matsuzawa M, Abe M, Horibe S, Sakai J. The effect of reduction on the mechanical properties of CeO_2 doped tetragonal zirconia ceramics. Acta Mater 2004;52:1675–82.
[6] Nawa M, Nakamoto S, Sekino T, Niihara K. Tough and strong Ce-TZP/alumina nanocomposites doped with titania. Ceram Int 1998;24:497–506.
[7] Panasonic Biomedical: http://www.die-modellmacher.de/Nano-ZR
[8] Apel E, Ritzberger C, Courtois N, Reveron H, Chevalier J, Schweiger M, et al. Introduction to a tough, strong and stable Ce-TZP/$MgAl_2O_4$ composite for biomedical applications. J Eur Ceram Soc 2012;32:2697–703.
[9] Cutler RA, Lindemann JM, Ulvensøen JH, Lange HI. Damage-resistant SrO-doped Ce-TZP/AI_2O_3 composites. Mater Des 1994;15:123–33.
[10] Ori S, Kojima T, Hara T, Uekawa N, Kakegawa K. Fabrication of Ce-TZP/β-hexaaluminate composites using amorphous precursor of the second phase. J Ceram Soc Jpn 2012;120:111–5.
[11] Miura M, Hongoh H, Yogo T, Hirano S, Fujll T. Formation of plate-like lanthanum-β-aluminate crystal in Ce-TZP matrix. J Mater Sci 1994;29:262–8.
[12] Tsukuma K. Conversion from -$Ce_2O_3$11Al_2O_3 to -Al_2O_3 in tetragonal ZrO_2 matrix. J Am Ceram Soc 2000;83:3219–21.
[13] Yamaguchi T, Sakamoto W, Yogo T, Fujii T, Hirano S. In situ formation of Ce-TZP/Ba-hexaaluminate composites. J Ceram Soc Jpn 1999;9:814–916.
[14] Tsai OF, Chon U, Ramachandran N, Shetty DK. Transformation plasticity and toughening in CeO_2-partially-stabilized zirconia–alumina (Ce-TZP/Al_2O_3) composites doped with MnO. J Am Ceram Soc 1992;75:1229–38.
[15] Kern F. A comparison of microstructure and mechanical properties of 12Ce-TZP reinforced with alumina and in situ formed strontium- or lanthanum-hexaaluminate precipitates. J Eur Ceram Soc 2014;34:413–23.
[16] Palmero P, Fornabaio M, Montanaro L, Reveron H, Esnouf C, Chevalier J. Towards long lasting zirconia-based composite for dental implants. Part I: innovative synthesis, microstructural characterization and in-vitro stability. Biomaterials 2014;50:38–46.
[17] http://www.dkkk.co.jp/english
[18] Palmero P, Naglieri V, Chevalier J, Fantozzi G, Montanaro L. Alumina-based nanocomposites obtained by doping with inorganic salt solutions: application to immiscible and reactive systems. J Eur Ceram Soc 2009;29:59–66.
[19] http://www.tosoh.com/our-products/advanced-materials/zirconia-grinding–dispersion-media
[20] Toraya H, Yoshimura M, Somiya S. Calibration curve for quantitative analysis of the monoclinic–tetragonal ZrO_2 system by X-ray diffraction. J Am Ceram Soc 1984;67:C119–21.
[21] Fengqiu T. Effect of dispersants on surface chemical properties of nano-zirconia suspensions. Ceram Int 2000;26:93–7.
[22] Greenwood R, Bergstrom L. Electroacoustic and rheological properties of aqueous Ce-ZrO_2 (Ce-TZP) suspensions. J Eur Ceram Soc 1997;17:537–48.
[23] Douy A, Capron M. Crystallization of spray-dried amorphous precursors in the SrO–Al_2O_3 system: a DSC study. J Eur Ceram Soc 2003;23:2075–81.
[24] Reyes-Morel PE, Chen IW. Transformation plasticity of CeO_2-stabilized tetragonal zirconia polycrystals: I. Stress assistance and autocatalysis. J Am Ceram Soc 1988;71:343–53.